Coal polymer composites prepared by fused deposition modeling (FDM) 3D printing

*Shuyang Zhang[1], Muhammad Zia ur Rehman[2], Samarthya Bhagia[3], Harry M. Meyer, III[4], Hsin Wang[5], Kalsoom Akhtar[2], Arthur J. Ragauskas[1,3,6]**

[1] Department of Chemical and Biomolecular Engineering, The University of Tennessee, Knoxville, TN 37996, USA

[2] Industrial Biotechnology Division, National Institute for Biotechnology and Genetic Engineering Constituent College (NIBGE-C) of Pakistan Institute of Engineering and Applied Sciences, 38000, Faisalabad, Punjab, Pakistan

[3]Joint Institute for Biological Sciences, Biosciences Division, Oak Ridge National Laboratory, Oak Ridge, TN 37831, USA

[4]Chemical Sciences Division, Oak Ridge National Laboratory, Oak Ridge, TN 37831, USA

[5]Materials Science and Technology Division, Oak Ridge National Laboratory, Oak Ridge, TN 37831, USA

[6]Department of Forestry, Wildlife and Fisheries, Center for Renewable Carbon, The University of Tennessee Institution of Agriculture, Knoxville, TN 37996, USA

Abstract

Coal is a vital energy resource worldwide, but pollutants and greenhouse gases from its combustion causes environmental problems. To explore the non-combustion approach to utilize and valorize coal, anthracite or lignite were blended with polyamide 12 (PA 12) through FDM printing in this work and compared in the composites. By adding lignite, Young's modulus improved with increasing loading while tensile strength increased at 20 wt% (44.6 MPa) and slightly decreased at 50 wt% (40.4 MPa), compared to that of neat PA 12 (42.6 MPa). By contrast, the addition of anthracite decreased the tensile strength, Young's modulus and elongation at break at all loadings. Rheology test and morphology analysis from SEM suggested that the interfacial differences between fillers (anthracite and lignite) and PA 12 may have cause the differences in tensile properties. In addition, the printed lignite composites showed improved thermal conductivity (~ twofold), indicating lignite demonstrates the potential to build functional composites. This work provides a strategy to use lignite in composites by 3D printing for value-added products and reduces the demand for petroleum-based polymers. Our approach divers lignite from combustion processes and alleviates the negative impact of lignite use on the environment.

Keywords,

3D printing, Fused deposition modeling, Coal polymer composites

Introduction

Coal has long been used as an energy resource for heat and electricity. However, the emissions from its combustion result in pollution and greenhouse gas emissions. Many approaches demonstrated the economic value of coal-based materials when diverted from direct combustion for energy. For example, coal has been converted to carbon fiber[1, 2], activated carbon[3-5], graphene[6-8] and carbon membrane[9], which can be further utilized in battery[9-13], catalyst[14], pollutant adsorption[15-17] and energy storage[4, 18]. In these reports, untreated coal was subjected to extreme thermal or chemical treatment to obtain the desired microstructure, which involves high-energy costs or chemical pollution that may also cause environmental problems. Some studies have taken advantage of raw coal as fillers to manufacture polymer composites[19]. Polok-Rubiniec et al. blended untreated anthracite with polypropylene for composites and reported an increase in Young's modulus on the addition of anthracite[20]. Tan et al. prepared surface-modified anthracite with higher hydrophobicity and blended it with styrene-butadiene rubber (SBR). The mechanical properties and thermal stability were increased with a modest loading of modified anthracite[21]. In another report, Tan et al. modified low-rank coal slime by surfactants and added it to SBR. The tensile strength of the composites with sodium dodecylbenzene sulfonate-modified coal exceeded that of SBR composites with a commercial filler (Carbon black N660)[22]. Phillips et al. studied the flexural and tensile behavior of three types of bituminous coal on high-density polyethylene-coal composites. Flexural strength reached a maximum at 30% loading, and tensile strength decreased with coal as the filler. The addition of a coupling agent did not affect the mechanical properties due to the low abundance of hydroxyl sites in coal[23]. These reports indicate that the surface chemistry of coal particles strongly affects the interactions in coal-based composites. Therefore, from the view of the surface chemistry of coals, the coal species may play an important role in coal composites preparation. Coal can be categorized into different ranks as peat, lignite, subbituminous coal, bituminous coal, and anthracite, according to the carbon/aromatic density, heat contents, and oxygen contents, etc.[24]. Different coal species may affect coal composites in different ways in terms of chemical differences (Fig 1a). Thus, coal species should be carefully selected for producing coal-polymer composites (CPC) with higher value.

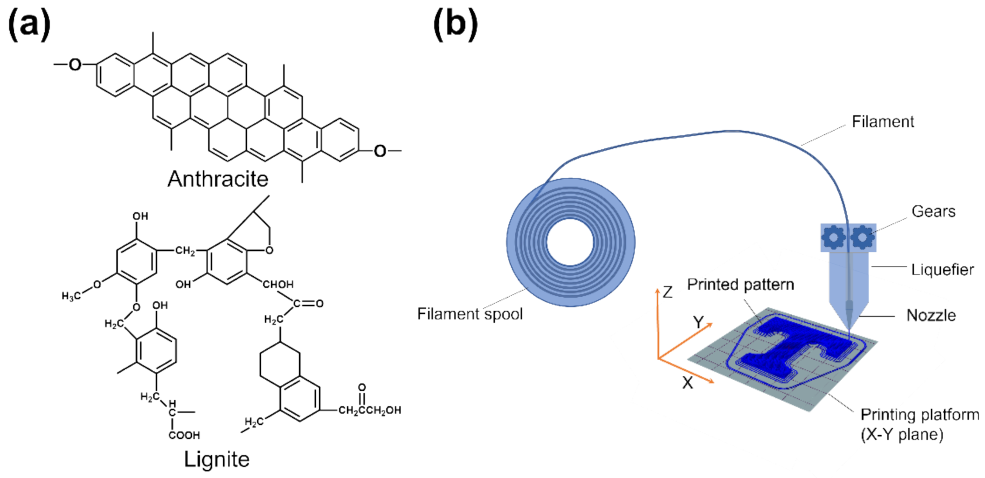

Fig. 1 (a) Structure comparison between anthracite and lignite. Redrawn according to Ref. [24], copyright 2011 Energy & Environmental Science; (b) Mechanism of FDM, copyright 2020 RSC Advances

Recently, three-dimensional printing (3D printing) has been intensively studied in polymer composites[25]. The target items can be built layer-by-layer with a 3D printer. The mold-free manufacturing methods allow complex hierarchy, which can further extend the functions of the composites. Several techniques, including but not limited to fused depositional modeling (FDM), stereolithography (SLA)/ digital light processing (DLP), and selective laser sintering (SLS), can be used to prepare polymer composites [25, 26]. The most widely used technique is FDM for its low cost and multi-material capability[27]. In FDM, the prepared filaments are fed into a liquefier that melts the polymer and extrudes roads through a nozzle (Fig. 1b)[26]. Parameters like the temperature of the nozzle and printing bed, printing speed, fill%, and filling pattern can be adjusted depending on the need. FDM has been demonstrated to produce functional polymer composites for thermal conductivity[28], electrical conductivity[29, 30], and shape memory effect[31-33].

This work explored lignite and anthracite as fillers in coal composites by FDM. Polyamide was chosen as the polymer matrix according to a previous report which suggested the amide group may contribute to the interactions between polymer matrix and coal particles[34]. PA 12 was selected because it has the lowest water adsorption among all PAs[35] and is widely used in FDM and SLS. The two types of coal were compared as a filler for 3D-printed composites in terms of chemical structure, interaction with PA 12, and the corresponding mechanical performance and morphology to understand the relationship between chemical structures and the resultant composite properties, thereby guiding the research in building coal composite.

2. Materials and Methods

2.1 Materials

Polyamide 12 (PA 12) pellets (viscosity number of 230 mL/g) was purchased from Scientific Polymer Products Inc. (New York, US). No. 4 anthracite coal was a kind gift from Blaschak Coal Corp (Mahanoy City, PA). Raw lignite was collected from the Salt Range of Punjab province in Pakistan. More details of the lignite are shown in the supporting information (Table S1 and Table S2). Both anthracite and lignite particles were ground with a Masuko supermasscolloider for 5 passes at 0 μm, 20 passes at -100 μm, and 5 passes at -200 μm (Saitama-pref, Japan). Details of the friction grinder are available elsewhere[36]. The size distribution of lignite and anthracite was measured by laser refraction on Malvern S3500, as shown in Fig 2.

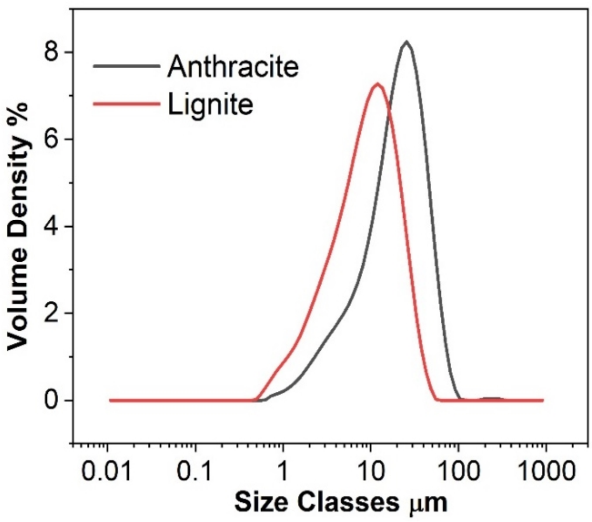

Fig 2. Size distribution of the anthracite and lignite

2.2 Preparation of the coal composite filaments

The coal particles (lignite or anthracite) and PA 12 pellets were dried at 45 ^{o}C in a vacuum oven overnight before the blending. Then the coal particles were blended with PA 12 respectively in Thermo Scientific HAAKE MiniLab II twin-screw extruder equipped with a 1.5 mm die at 220 ^{o}C with a rotating speed of 70 rpm. The obtained composite filament was cut to small particles (~3-5 mm) by a pelletizer and extruded with the extruder for the second time at 220 ^{o}C with 50 rpm. According to the weight contents of the coal particles, the composites were marked as Lig-X or An-X or Lig-X & An-Y (ternary blend), in which X or Y represents the weight concentration of coal particles in the composites. For example, An- 5 represents that 5 wt% of anthracite was contained in the PA composite, Lig-20% & An-5% represent that 20 wt% of lignite and 5 wt% of anthracite was added in the composite. Pure PA 12 also underwent the same procedure to prepare the neat filament and was labeled as PA.

2.3 3D printing of the composite filament

The composite filaments with a diameter of ~1.75 mm were mounted on an FDM printer, MakerGear M2, for 3D printing with a nozzle diameter of 0.35 mm. The hot end temperature was set as 250 ^{o}C while the temperature of the printing bed (coated with polyimide tape) was set as 110 ^{o}C. All the items are printed with 100% infill and 45^{o} of the rectilinear pattern. Other details in FDM printing (e.g., layer height, printing speed, etc.) can be found in the supporting information in Fig S1.

2.4 Characterizations

2.4.1 Fourier-transform infrared spectroscopy (FTIR)

The FTIR-ATR spectra were acquired on a Perkin Elmer FTIR-ATR spectrometer II at 18 ^{o}C for coal samples and the printed composites. Each spectrum had 16 scans at 4 cm^{-1} resolution from 4000 cm^{-1} to 600 cm^{-1}.

2.4.2 Tensile testing

The composite filaments were printed to dog-bone shape (Type V) for tensile tests according to ASTM 638[37]. The tensile sample was drawn uniaxially on a universal testing machine (Instron-5567, Instron Co.) with a 30 kN load cell under a constant crosshead speed of 10 mm/min. The tensile force was recorded, and the nominal tensile stress was generated according to the sample size. The tensile strength values were marked as the maximum tensile stress during a tensile process, while Young's modulus values were obtained by linear fitting of the stress-strain curve within the linear strain region from 0.1% - 0.5%.

2.4.3 Rheology test

All samples for rheology testing were pressed at 220 ^{o}C using pellets cut from the second-extruded filaments to melt and form disks with a diameter of 25 mm and thickness of 2 mm. The tests were performed on a rotational rheometer (ARES-G2, TA Instruments.) equipped with a 25 mm parallel-plate geometry with 1000 μm as the gap. The frequency sweep was conducted at 230 ^{o}C with the shear frequency range from 0.0628 rad/s to 628 rad/s at 1% strain (in the linear viscoelastic region).

2.4.4 Scanning electron microscopy (SEM)

The morphological analysis was taken on the cross-section of the second-extruded filaments. The filament was first soaked in liquid nitrogen for 30 min and then fractured cryogenically and mounted on stubs. The cross-section was coated with a thin layer of gold before the observation using an SEM instrument (Zeiss EVO MA15). The acceleration voltage was set to 5 kV.

2.4.5 X-ray photoelectron spectroscopy (XPS)

X-ray photoelectron spectroscopy (XPS) was performed using a Thermo Scientific (Waltham, MA, USA) Model K-Alpha XPS instrument. The instrument utilizes monochromated, micro-focused Al K α X-rays (1486.6 eV) with a variable spot size (i.e., 30-400 μm). Analyses of the sample were performed with the 400 μm X-ray spot size for maximum signal and an average surface composition over the largest possible area. The instrument has a hemispherical electron energy analyzer equipped with a 128-channel detector system. Base pressure in the analysis chamber was typically 2×10^{-9} mbar or lower. The sample was mounted by dispersing the powder onto double-sided tape fixed to a clean glass slide. Survey spectra (pass energy = 200 eV) were acquired for qualitative and quantitative analysis, and high-resolution core-level spectra (pass energy = 50 eV) were acquired for detailed chemical state analysis. All spectra were acquired with the charge neutralization flood gun turned on to maintain a stable analysis condition. The flood gun uses a combination of low-energy electrons and argon ions for optimum charge compensation. The typical pressure in the analysis chamber with the flood gun operating was 2×10^{-5} Pa. Data were collected and processed using the Thermo Scientific Avantage XPS software package (v.5.96). Peak fitting was performed using mixed Gaussian/Lorentzian peak shapes and a Shirley/Smart type background.

2.4.6 XRD

The X-ray diffraction for the lignite particle was recorded through a PANalytical Empyrean X-ray diffractometer for lignite powder. A Cu Kα source was used with the wavelength λ=0.154 nm (generator voltage of 45 kV and tube current 40 mA). The spectrum was recorded with the 2θ range of 10°– 60°.

2.4.7 Thermal conductivity test

Thermal conductivity was measured using the transient plane source (TPS) method, which is also known as the Hot Disk technique. The sensor/heater is a thin, double-spiral nickel disk sandwiched between Kapton insulation films (Shown in Fig S2). The senor was placed between two identical specimens during the measurement, and constant power heating from 5-40 seconds (depending on thermal conductivity) was applied. The sensor measures the interface temperature as a function of time. The transient was directly used to calculate the thermal conductivity of the material. For this work, a Hot Disk sensor with a radius of 3.189 mm was used, and the heating was 20 mW for 10 seconds.

3 Results and discussion:

3.1. Chemical difference between anthracite and lignite

Anthracite and lignite were characterized for the chemical difference by FTIR before blending with PA 12 shown in Fig 3. For both coal species, there are mainly four spectral regions of interest including hydroxyl, aliphatic, mineral, and aromatic, as shown in Fig 2[38]. For lignite, the stretching of free hydroxyl groups was assigned to the peaks at 3691, 3650, and 3619 cm^{-1} and the intermolecular bonded hydroxyl group at 3366 cm^{-1}. The two peaks at 2919 and 2844 cm^{-1} were attributed to the stretching of $-CH_2$ and CH_3, and the peak at 1700 cm^{-1} was related to the stretching of C=O. The strong peaks in the region of 1000-1200 cm^{-1} were attributed to the metal-O bonding compounded in the coal due to clay minerals such as quartz, kaolinite, and illite montmorillonite during the geological formation[39]. Aromatic -CH's bending showed strong peaks at 797 (3 substitutions) and 749 cm^{-1} (2 substitutions). With respect to anthracite, the peaks at hydroxyl, aliphatic, and mineral regions can also be assigned (Table 1), but they have weaker peaks compared to the strong absorption at the aromatic region. The results correspond with the predicted structures of lignite and anthracite in the literature, as shown in Fig 1a that there are more oxygen-contained functional groups and aliphatic structures in lignite, while anthracite has high aromatic structure content as well as carbon density[24]. All the assignments of the peaks can be found in Table 1. The FTIR results of the printed samples (PA/lignite and PA/Anthracite) are also obtained, as shown in Fig S4.

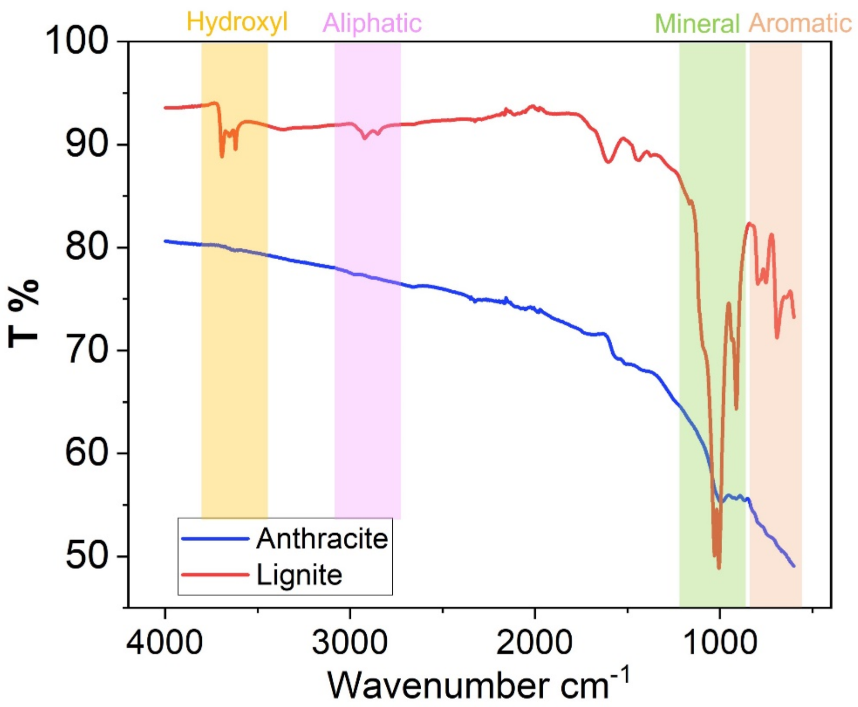

Fig 3. FTIR spectra of anthracite and lignite particles

Table 1. Peak assignment of the groups in lignite and anthracite by FTIR

Structures		Wavenumber (cm^{-1}) Lignite	Anthracite
Aromatic -CH out of plane	Aromatics with 2 substitutions	749[39]	748[40]
	Aromatics with 3 substitutions	797[39]	792[40]
	Aromatics with 4 substitutions		827[40]
	Aromatics with 5 substitutions		871[40]
X-O bonding in minerals, X represent metal atoms (Si, Al et al.)		1007, 1030, 1114, 1167[39]	1001, 1167[40]
vibration of C-O, stretching of -OH in phenoxy structures, ethers		1294[39]	1252[41]
bending of $-CH_3$ and $-CH_2$		1373(Symmetric) [42], 1445 (Asymmetric)[42-44]	1430[45]
C=C stretching		1617[43]	1567[24]

C=O stretching	1700 (-COOH)	1736 (aromatic)
Stretching of aliphatic -CH_x	2844, 2919	2880, 2997
intermolecular bonded O-H	3366	3317
free -OH	3619, 3650, 3691	3620

3.2 Tensile performance of 3D-printed PA/Anthracite and PA/Lignite composites

Anthracite is the highest rank of coal which is expected to reinforce the composites[20, 21]. Therefore, the tensile performance was first measured for the PA/anthracite composites. The tensile curves in Fig 4a show that the elongation at break (EB) and tensile strength decreases significantly. From the collected results in Fig 4b, EB dropped from ~83% (PA) to ~26%, ~11%, and ~8%, while the tensile strength decreases from 42.6 MPa to 38.2 MPa, 35.5MPa, and 29.9 MPa, respectively, with increasing the filling contents of anthracite in the printed samples. The Young's modulus also decreases from 1.66 GPa (PA) to 1.38 GPa (An-5%), 1.40 GPa (An-10%) and 1.19 GPa (An-20%). This observation is an unexpected result granted that anthracite could be a reinforced filler in other reports[20, 21], which might be due to the poor interaction between anthracite and PA 12.

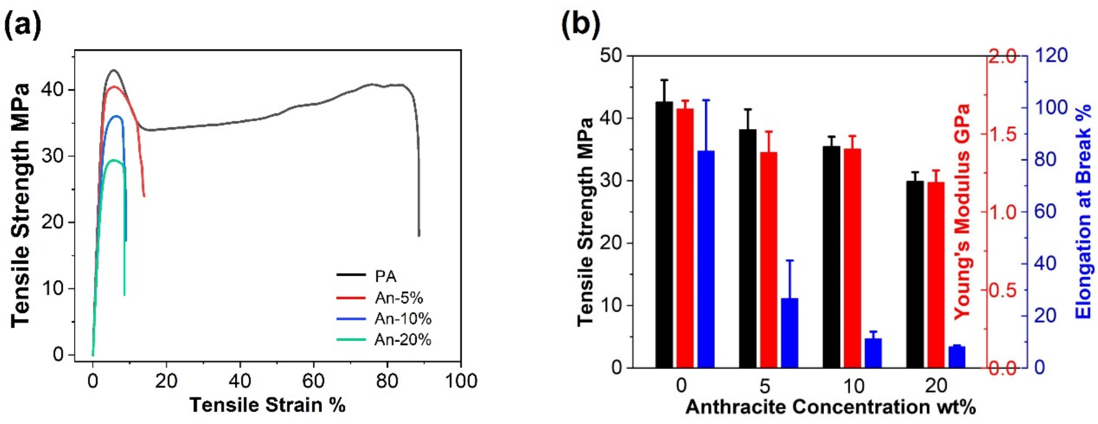

Fig. 4 a. Selected tensile curves of the PA/Anthracite composites with various anthracite concentrations. b. Comparisons for Tensile strength, Young's modulus, and elongation at break among PA/Anthracite composites.

For lignite, the addition of lignite also leads to a lower EB, as seen from Fig 5a. However, the tensile strength level off for the composites with more lignite loading than that of anthracite composites. As shown in Fig 5b, EB of PA/lignite composite (44% for Lig-5%, 15% for Lig-10%, 24% for Lig-20%, and 3% for Lig-50%) are all lower than that of pure PA (~83%). the tensile strength is respectively 42.6 MPa (PA), 42.5 MPa (Lig-5%), 39.1 MPa (Lig-10%), 44.6 MPa (Lig-20%) and 40.4 MPa (Lig-50%). Some notable results include that Lignite-20% had a higher tensile strength than pure PA, and the 50% of lignite contents can still retain tensile strength of 40.4 MPa, which may come from the interactions between oxygen-contained functional groups on lignite and the amide bond of PA. The slightly changed tensile strength value implied lignite could replace PA without sacrifice the tensile strength when lignite <50 wt%. Young's modulus increase as more lignite is added from 1.66 GPa (pure PA) to 1.69 GPa (Lig-5%), 1.72 GPa (Lig-10%), 1.73 GPa (Lig-20%), 2.43 GPa (Lig-50%). Based on the tensile results, the Lig-20% composites had higher tensile strength and Young's modulus compared to the pure PA sample, which could be reinforced PA composites with a moderate EB (~24%). Lignite-50% composites own a 46%-improved Young's modulus with a tensile strength of 40.4 MPa could also be a replacement of pure PA in FDM 3D printing products.

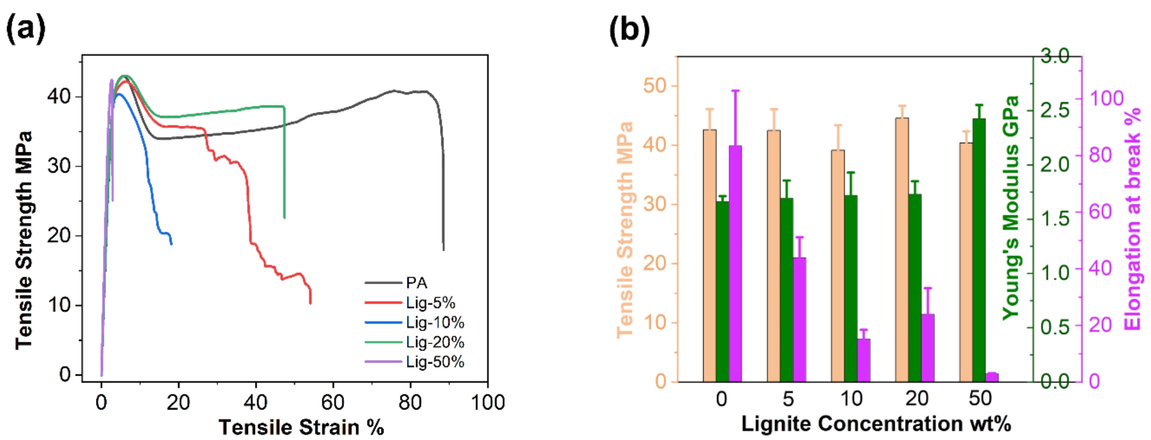

Fig. 5 a. Selected tensile curves of the PA/Lignite composites with various lignite concentration. b. Comparisons for tensile strength, Young's modulus, and elongation at break among PA/Lignite composites.

3.3 Rheology tests to understand the interactions between coal particles and the PA matrix

Given that tensile test results implied differences in tensile behavior between anthracite-PA and lignite-PA, rheology was carried out to understand the interactions in the composite melt. With the addition of fillers (lignite and anthracite in the current study), the rheology performance may also be influenced, which will give the information of the interactions between fillers and the polymer matrix. The log of storage modulus (log G') plots as a function of the log of angular frequency (log ω) are given in Fig 7a. At high shear frequency, all the samples fall into a similar range of log G' because large units (e.g., molecular chains) do not have enough time to relax; thus, small units (like segments, carbon-carbon bonding) dominate the rheological performance, leading to a similar storage. At low frequency, the rheology performance is more related to the large-scale structures, for example, the polymer network, which will be useful to understand the relationship between the fillers and the polymer matrix[46]. All coal-filled melts have higher G' at low frequency (< 30 rad/s) compared to pure PA. Specifically, anthracite-filled melt increases the storage modulus with a limited degree, while adding lignite significantly improves the storage at low angle frequency with increasing contents. According to existed reports, the increase of G' at low frequency could be attributed to the particle-polymer interactions, particle-particle interactions that enhance the melt network as a whole, or the hydrodynamic effect by adding particles[46]. The loss tangent (tanδ) can also be obtained from $\tan\delta = G''/G'$. Given that G' represents the elastic behavior while G" represents the viscous behavior, the loss tangent could indicate if the melt is more elastic or viscous at a different frequency. As we can see from Fig 7b, the incorporation of anthracite and lignite decreases the loss tangent except at high frequency (>100 rad/s), which means both the two coal particles could enhance the elastic behaviors the PA/coal melts. Within the frequency range, lignite-filled melt had a lower loss tangent than that of anthracite-filled melt, which implies higher elastic behavior by adding lignite. From the above data, a conclusion that lignite benefits the interactions with PA 12 could be obtained compared to the pure PA sample from the G' and tanδ plots while anthracite has less influence as lignite at given size distribution. To understand the enhanced interaction, PLS analysis was done by correlating FTIR with rheology data for lignite composites. According to the variable importance plot from PLS analysis data (Fig S5), the first three absorbances most contributed to the rheology behavior are at 1032 cm^{-1}, 1008 cm^{-1}, and 1632 cm^{-1} (circled as red). The two peaks at 1032 cm^{-1} and 1008 cm^{-1} are related to the X-O bonding (X represents Si or Al etc.) in lignite, and 1632 cm^{-1} is attributed to Amide I (C=O or C-N stretching) in PA 12 skeleton, which imply possible bonding might be formed between these groups. From this point, the enhanced interactions in the melt elasticity, thereby maintaining comparable tensite strength of lignite composites to PA 12.

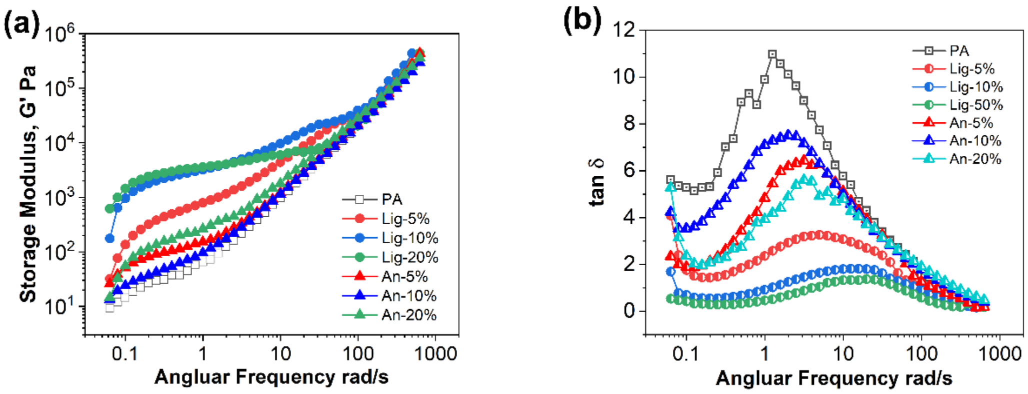

Fig 7. Rheology tests results. (a). Storage modulus(G') vs angular frequency; (b) Loss tangent (tanδ) vs angular frequency

3.4 Morphology analysis for the composites

The interaction between filler and the polymer matrix can also be illustrated by the compatibility analyzed and compared from the morphology difference in SEM. The poor interaction between anthracite and PA resulted in holes and pits after the cryogenically fractured cross-sections, as seen for An-10% in Fig 8 (some of them are marked by red circle) and Fig S4. The pits in the SEM images are shown as the grey area (Fig 8b, c, d) due to the detachment of anthracite particles. The apparent gap between the anthracite particle and the matrix also implies poor interaction, as shown in Fig 8d (pointed by yellow arrow). The holes were formed in a similar way but may be caused by fillers deeper buried in the polymer matrix that was pulled out during the cryogenically fracture. By contrast, at the same loading concentration of 10 wt%, lignite showed few detachment spots (marked by red circle) on the cross-section, shown in Fig 9a and Fig 9b. The lignite particles were well-bonded with polymer matrix, as shown in Fig 9c (yellow arrow). The good interaction between lignite and PA 12 that leads to few detachments can also be proved by the cross-section of Lig-20% as shown in Fig S5.

The morphological difference is also in accord with the rheology test that lignite favors the interaction of anthracite in the PA matrix.

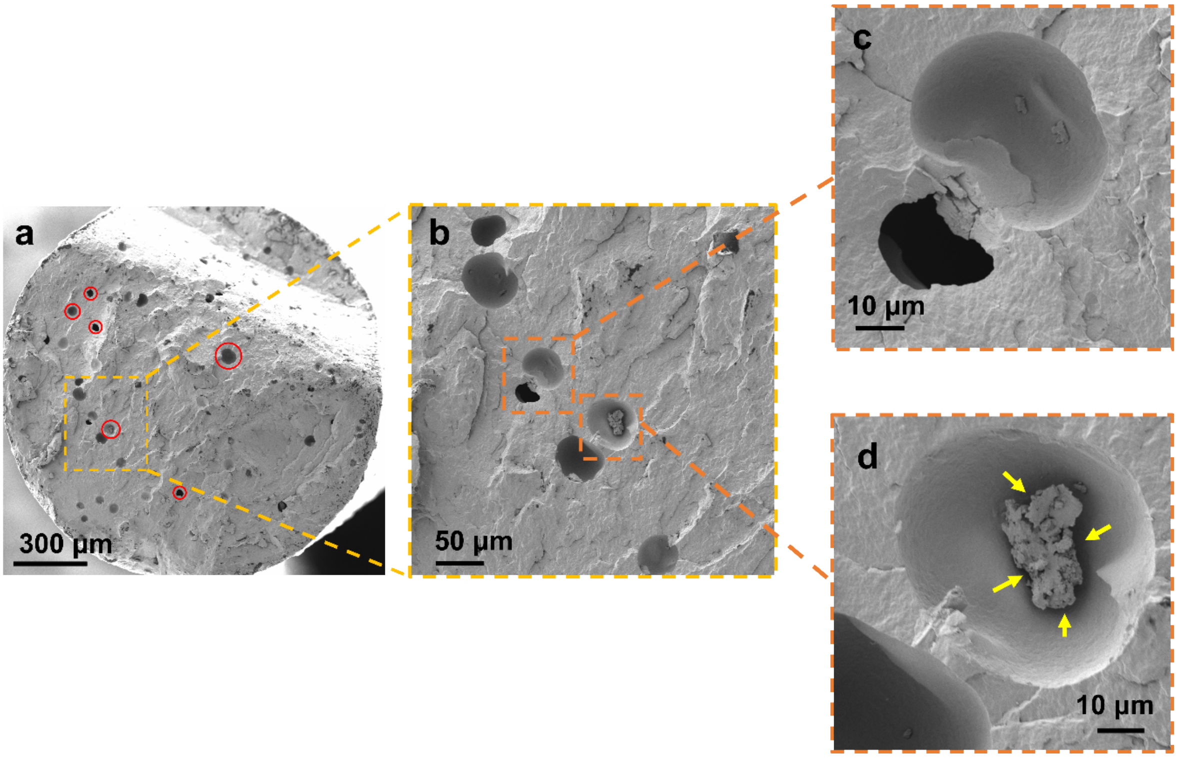

Fig 8. Cross-section SEM images of the PA/anthracite filament. Scale bar: (a) 300 μm; (b) 50 μm; (c) 10 μm; (d) 10 μm

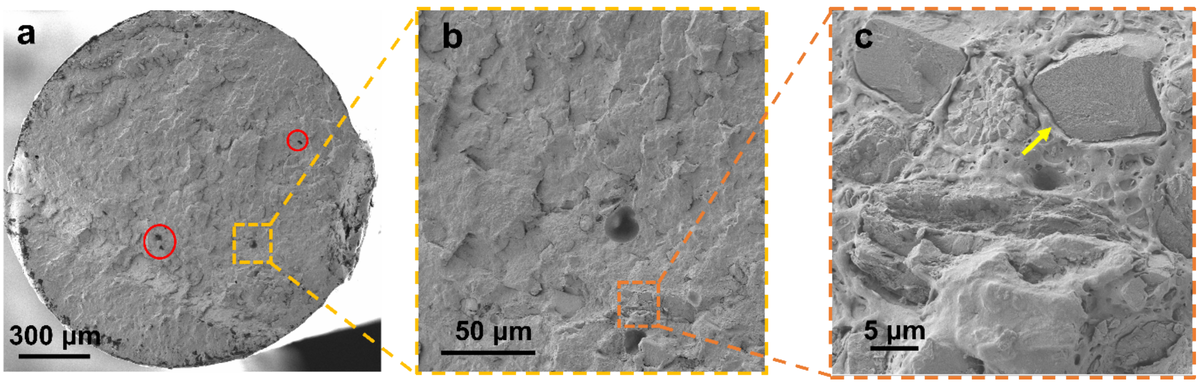

Fig 9. Cross-section SEM images of the PA/lignite filament. Scale bar: (a) 300 μm; (b) 50 μm; (c) 5 μm

Fig 10. Tensile performance between PA, Lig-20%, An-5%, Lig-50% and Lig-20%&An-5%

3.6. Exploring the thermal conductivity of the lignite composite

As lignite can be blended in the composites at high concentration, the other components in lignite may also affect the performance of the lignite composites. Raw lignite is a mixture of various compounds including many elements as shown in XPS results (Fig S6 and Table S1). These elements existed as metal oxides, which may be used for further functional applications of the coal composites. For example, Al_2O_3 can be found in lignite by XPS and XRD (Fig S7). The addition of lignite could increase the thermal conductivity of composite due to the natural heat conduction properties of Al_2O_3 [47]. The thermal conductivity was measured for pure PA sample and Lignite-50%, as shown in Table 2. The thermal conductivity of lignite-50% (0.1927 W/mK) is ~2-time of that for PA (0.1041 W/mK), which implied the potential for lignite as the thermal-conductive filler. With a tensile strength of 40.4 MPa and Young's modulus of 2.43 GPa, Lig-50% could be studied to improve thermal transmission for thermal-conductive materials such as electronic components[48].

Table 2. Thermal conductivity comparison between printed samples from PA and Lig-50%

Sample	PA	Lig-50%
Thermal conductivity, W/mK	0.1041 ± 0.0008	0.1927±0.0012

Conclusion

The current study investigated anthracite and lignite as the filler in polymer composites with PA 12. FTIR spectra showed strong oxygen-contained functional groups in lignite and strong absorbance in the aromatic region for anthracite. Tensile test results showed a decrease in tensile strength, Young's modulus, and EB with the addition of anthracite to PA 12, indicating poor interaction between them, which was also supported by the rheological and morphological analysis. By contrast, adding lignite to PA 12 maintained a comparable tensile strength up to 50%. Young's modulus remains comparable as lignite was added up to 20 wt% and significantly improved when adding 50 wt%. The morphological analysis also supported the good interaction between lignite and PA12. Rheology test results showed that lignite affected the relaxation of the polymer network in terms of higher melt elasticity. Along with the results from PLS, this may be attributed to the filler-polymer interaction that comes from the possible bonding between PA 12 and the surface functional groups from lignite. Lignite also showed improved thermal conductivity at 50 wt%. Based on these results, lignite could be an inexpensive filler for PA composites in FDM 3D printing to replace PA products at a proper feeding ratio. The improved thermal conductivity of the composites could also extend the application of lignite for further building functional composites. This work provided a strategy to use lignite in composite by 3D printing for value-added products, which may extend the lignite utilization to non-combustion approaches to reduce the negative impact on the environment.

Reference

[1] M. Guo, J. Guo, D. Jia, H. Zhao, Z. Sun, X. Song, Y. Li, Coal derived porous carbon fibers with tunable internal channels for flexible electrodes and organic matter absorption, Journal of Materials Chemistry A 3(42) (2015) 21178-21184.
[2] H. Zhao, L. Wang, D. Jia, W. Xia, J. Li, Z. Guo, Coal based activated carbon nanofibers prepared by electrospinning, Journal of Materials Chemistry A 2(24) (2014) 9338-9344.
[3] H.-C. Lee, N. Byamba-Ochir, W.-G. Shim, M. Balathanigaimani, H. Moon, High-performance super capacitors based on activated anthracite with controlled porosity, Journal of Power Sources 275 (2015) 668-674.
[4] B.-L. Xing, H. Guo, L.-J. Chen, Z.-F. Chen, C.-X. Zhang, G.-X. Huang, W. Xie, J.-L. Yu, Lignite-derived high surface area mesoporous activated carbons for electrochemical capacitors, Fuel Processing Technology 138 (2015) 734-742.
[5] S. Gao, L. Liu, Y. Tang, D. Jia, Z. Zhao, Y. Wang, Coal based magnetic activated carbon as a high performance adsorbent for methylene blue, Journal of Porous Materials 23(4) (2016) 877-884.
[6] A. Kovalchuk, K. Huang, C. Xiang, A.A. Martí, J.M. Tour, Luminescent polymer composite films containing coal-derived graphene quantum dots, ACS applied materials & interfaces 7(47) (2015) 26063-26068.
[7] J. Zhu, S. Zhang, L. Wang, D. Jia, M. Xu, Z. Zhao, J. Qiu, L. Jia, Engineering cross-linking by coal-based graphene quantum dots toward tough, flexible, and hydrophobic electrospun carbon nanofiber fabrics, Carbon 129 (2018) 54-62.
[8] B. Xing, H. Zeng, G. Huang, C. Zhang, R. Yuan, Y. Cao, Z. Chen, J. Yu, Porous graphene prepared from anthracite as high performance anode materials for lithium-ion battery applications, Journal of Alloys and Compounds 779 (2019) 202-211.
[9] M. Kang, H. Zhao, J. Ye, W. Song, H. Shen, J. Mi, Z. Li, Adsorption dominant sodium storage in three-dimensional coal-based graphite microcrystal/graphene composites, Journal of Materials Chemistry A 7(13) (2019) 7565-7572.
[10] J. Li, Y. Cao, L. Wang, D. Jia, Cost-effective synthesis of bamboo-structure carbon nanotubes from coal for reversible lithium storage, RSC advances 7(55) (2017) 34770-34775.
[11] X.-K. Ding, L.-L. Zhang, X.-L. Yang, H. Fang, Y.-X. Zhou, J.-Q. Wang, D. Ma, Anthracite-derived dual-phase carbon-coated Li3V2 (PO4) 3 as high-performance cathode material for lithium ion batteries, ACS applied materials & interfaces 9(49) (2017) 42788-42796.

[12] H. Lu, S. Sun, L. Xiao, J. Qian, X. Ai, H. Yang, A.-H. Lu, Y. Cao, High-capacity hard carbon pyrolyzed from subbituminous coal as anode for sodium-ion batteries, ACS Applied Energy Materials 2(1) (2019) 729-735.
[13] S. Gao, Y. Tang, Y. Gao, L. Liu, H. Zhao, X. Li, X. Wang, Highly crystalized Co2Mo3O8 hexagonal nanoplates interconnected by coal-derived carbon via the molten-salt-assisted method for competitive Li-ion battery anodes, ACS applied materials & interfaces 11(7) (2019) 7006-7013.
[14] S. Gao, Y. Tang, L. Wang, L. Liu, D. Jia, Z. Zhao, NiFe nanoalloys in-situ immobilized on coal based activated carbons through one-step pyrolysis as magnetically recoverable catalysts for reduction of 4-nitrophenol, Journal of Alloys and Compounds 702 (2017) 531-537.
[15] F.M. Mohamed, Z. Li, A.M. Zayed, Carbon nanotube impregnated anthracite (An/CNT) as a superior sorbent for azo dye removal, RSC Advances 10(43) (2020) 25586-25601.
[16] X.Q. Yang, K.W. Zhu, X.M. Yue, S.Q. Zhang, S. He, S. Komarneni, Porous solids by the pyrolysis of residue obtained after NaOH extraction of lignite, Journal of Porous Materials 25(3) (2018) 897-904.
[17] E.A. Mohamed, A.Q. Selim, S.A. Ahmed, L. Sellaoui, A. Bonilla-Petriciolet, A. Erto, Z. Li, Y. Li, M.K. Seliem, H2O2-activated anthracite impregnated with chitosan as a novel composite for Cr(VI) and methyl orange adsorption in single-compound and binary systems: Modeling and mechanism interpretation, Chemical Engineering Journal 380 (2020).
[18] X. Zhu, Q. Wang, S. Kang, J. Li, X. Jia, Coal-based ultrathin-wall graphitic porous carbon for high-performance form-stable phase change materials with enhanced thermal conductivity, Chemical Engineering Journal 395 (2020) 125112.
[19] Y.A. Al-Majali, C.T. Chirume, E.P. Marcum, D.A. Daramola, K.S. Kappagantula, J.P. Trembly, Coal-Filler-Based Thermoplastic Composites as Construction Materials: A New Sustainable End-Use Application, ACS Sustainable Chemistry & Engineering 7(19) (2019) 16870-16878.
[20] M. Polok-Rubiniec, A. Włodarczyk-Fligier, B. Chmielnicki, The Properties of a Polypropylene Matrix Composite with Anthracite Filler, vol. 66(No 1) (2021) 305-311-305-311.
[21] J.L. Tan, H.Z. Cheng, L.B. Wei, X.H. Gui, Thermal and mechanical enhancement of styrene-butadiene rubber by filling with modified anthracite coal, Journal of Applied Polymer Science 136(42) (2019).
[22] J. Tan, H. Cheng, L. Wei, C. Wei, Y. Xing, X. Gui, Using low-rank coal slime as an eco-friendly replacement for carbon black filler in styrene butadiene rubber, Journal of Cleaner Production 234 (2019) 949-960.
[23] L.N. Phillips, K.S. Kappagantula, J.P. Trembly, Mechanical performance of thermoplastic composites using bituminous coal as filler: Study of a potentially sustainable end-use application for Appalachian coal, Polymer Composites 40(2) (2019) 591-599.
[24] S. Vasireddy, B. Morreale, A. Cugini, C. Song, J.J. Spivey, Clean liquid fuels from direct coal liquefaction: chemistry, catalysis, technological status and challenges, Energy & Environmental Science 4(2) (2011) 311-345.
[25] S.C. Ligon, R. Liska, J. Stampfl, M. Gurr, R. Mülhaupt, Polymers for 3D Printing and Customized Additive Manufacturing, Chemical Reviews 117(15) (2017) 10212-10290.
[26] A. Ji, S. Zhang, S. Bhagia, C.G. Yoo, A.J. Ragauskas, 3D printing of biomass-derived composites: application and characterization approaches, RSC Adv. 10(37) (2020) 21698-21723.
[27] X. Wang, M. Jiang, Z. Zhou, J. Gou, D. Hui, 3D printing of polymer matrix composites: A review and prospective, Composites Part B: Engineering 110 (2017) 442-458.
[28] S. Waheed, J.M. Cabot, P. Smejkal, S. Farajikhah, S. Sayyar, P.C. Innis, S. Beirne, G. Barnsley, T.W. Lewis, M.C. Breadmore, Three-dimensional printing of abrasive, hard, and thermally conductive synthetic microdiamond–polymer composite using low-cost fused deposition modeling printer, ACS applied materials & interfaces 11(4) (2019) 4353-4363.
[29] G. Chen, N. Chen, Q. Wang, Preparation of poly (vinyl alcohol)/ionic liquid composites with improved processability and electrical conductivity for fused deposition modeling, Materials & design 157 (2018) 273-283.

[30] K. Gnanasekaran, T. Heijmans, S. Van Bennekom, H. Woldhuis, S. Wijnia, G. De With, H. Friedrich, 3D printing of CNT-and graphene-based conductive polymer nanocomposites by fused deposition modeling, Applied materials today 9 (2017) 21-28.
[31] C. Lin, J.X. Lv, Y.S. Li, F.H. Zhang, J.R. Li, Y.J. Liu, L.W. Liu, J.S. Leng, 4D-Printed Biodegradable and Remotely Controllable Shape Memory Occlusion Devices, Advanced Functional Materials 29(51) (2019).
[32] J.C. Wang, Z.G. Wang, Z.Y. Song, L.Q. Ren, Q.P. Liu, L. Ren, Biomimetic Shape-Color Double-Responsive 4D Printing, Advanced Materials Technologies 4(9) (2019).
[33] D.B. Chen, Q.P. Liu, Z.W. Han, J.Q. Zhang, H.L. Song, K.J. Wang, Z.Y. Song, S.F. Wen, Y. Zhou, C.Z. Yan, Y.S. Shi, 4D Printing Strain Self-Sensing and Temperature Self-Sensing Integrated Sensor-Actuator with Bioinspired Gradient Gaps, Advanced Science 7(13) (2020).
[34] W. Zou, J. Zhao, C. Sun, Adsorption of anionic polyacrylamide onto coal and kaolinite calculated from the extended DLVO theory using the van Oss-Chaudhury-Good theory, Polymers 10(2) (2018) 113.
[35] A. Touris, A. Turcios, E. Mintz, S.R. Pulugurtha, P. Thor, M. Jolly, U. Jalgaonkar, Effect of molecular weight and hydration on the tensile properties of polyamide 12, Results in Materials 8 (2020) 100149.
[36] S. Bhagia, N.C. Gallego, N. Hiremath, D.P. Harper, R.A. Lowden, R.R. Lowden, Y. Pu, U. Vaidya, S. Ozcan, A.J. Ragauskas, Fine grinding of thermoplastics by high speed friction grinding assisted by guar gum, Journal of Applied Polymer Science 138(32) (2021) 50797.
[37] ASTM D638-14, Standard Test Method for Tensile Properties of Plastics, ASTM International, West Conshohocken, PA, 2014, www.astm.org.
[38] J. Liu, Y. Jiang, W. Yao, X. Jiang, X. Jiang, Molecular characterization of Henan anthracite coal, Energy & Fuels 33(7) (2019) 6215-6225.
[39] L. Zhao, N. Guanhua, W. Hui, S. Qian, W. Gang, J. Bingyou, Z. Chao, Molecular structure characterization of lignite treated with ionic liquid via FTIR and XRD spectroscopy, Fuel 272 (2020) 117705.
[40] H. Guo, Y. Zhang, J. Zhang, Z. Huang, M.A. Urynowicz, W. Liang, Z. Han, J. Liu, Characterization of anthracite-degrading methanogenic microflora enriched from Qinshui Basin in China, Energy & Fuels 33(7) (2019) 6380-6389.
[41] Y. Zhang, J. Tan, X. Kang, H. Yu, R.L. Frost, Structure evolution characterization of Anyang anthracites via H2O2 oxidization and HF acidification, Spectrochimica Acta Part A: Molecular and Biomolecular Spectroscopy 130 (2014) 574-580.
[42] X. Qi, L. Chen, L. Zhang, C. Bai, H. Xin, Z. Rao, In situ FTIR study on real-time changes of active groups during lignite reaction under low oxygen concentration conditions, Journal of the Energy Institute 92(5) (2019) 1557-1566.
[43] X. Qi, D. Wang, H. Xin, G. Qi, In situ FTIR study of real-time changes of active groups during oxygen-free reaction of coal, Energy & Fuels 27(6) (2013) 3130-3136.
[44] L. Feng, G. Zhao, Y. Zhao, M. Zhao, J. Tang, Construction of the molecular structure model of the Shengli lignite using TG-GC/MS and FTIR spectrometry data, Fuel 203 (2017) 924-931.
[45] S. Liu, S. Sang, J. Ma, T. Wang, Y. Du, H. Fang, Effects of supercritical CO2 on micropores in bituminous and anthracite coal, Fuel 242 (2019) 96-108.
[46] S. Huang, Z. Liu, C. Yin, Y. Gao, Y. Wang, M. Yang, Gelation of attractive particles in polymer melt, Polymer 53(19) (2012) 4293-4299.
[47] M. Li, Y. Wan, Z. Gao, G. Xiong, X. Wang, C. Wan, H. Luo, Preparation and properties of polyamide 6 thermal conductive composites reinforced with fibers, Materials & Design 51 (2013) 257-261.
[48] Y. Zheng, R. Wang, X. Dong, L. Wu, X. Zhang, High Strength Conductive Polyamide 6 Nanocomposites Reinforced by Prebuilt Three-Dimensional Carbon Nanotube Networks, ACS Applied Materials & Interfaces 10(33) (2018) 28103-28111.